



Observations of Binary Stars with the Differential Speckle Survey Instrument. VIII. Measures of Metal-poor and Triple Stars from 2015 to 2018

Elliott P. Horch^{1,14,15} , Andrei Tokovinin² , Samuel A. Weiss^{1,14}, János Löbb¹, Dana I. Casetti-Dinescu^{1,3,4} ,
Nicole M. Granucci¹, Nicole M. Hess¹, Mark E. Everett⁵ , Gerard T. van Belle^{6,14} , Jennifer G. Winters^{7,14} ,
Daniel A. Nusdeo^{8,14}, Todd J. Henry^{9,14}, Steve B. Howell^{10,14} , Johanna K. Teske^{11,14}, Lea A. Hirsch^{12,14} ,
Nicholas J. Scott^{10,14} , Rachel A. Matson^{10,14} , and Stephen R. Kane¹³

¹ Department of Physics, Southern Connecticut State University, 501 Crescent Street, New Haven, CT 06515, USA; horche2@southernct.edu,
weiss4@southernct.edu, janos@lobb.com, danacasetti@gmail.com, granucci.nicole@gmail.com, hessn1@southernct.edu

² Cerro Tololo Inter-American Observatory, Casilla 603, La Serena, Chile; tokovinin@ctio.edu

³ Astronomical Institute of the Romanian Academy, str. Cutitul de Argint 5, Bucharest, Romania

⁴ Radiology and Biomedical Imaging, Yale School of Medicine, 300 Cedar Street, New Haven, 06519, USA

⁵ National Optical Astronomy Observatory, 950 North Cherry Avenue, Tucson, AZ 85719, USA; everett@noao.edu

⁶ Lowell Observatory, 1400 West Mars Hill Road, Flagstaff, AZ 86001, USA; gerard@lowell.edu

⁷ Harvard-Smithsonian Center for Astrophysics, 60 Garden Street, Cambridge, MA 02138, USA; winters@cfa.harvard.edu

⁸ Department of Physics and Astronomy, Georgia State University, 25 Park Place, Atlanta, GA 30302, USA; nusdeo@astro.gsu.edu

⁹ RECONS Institute, Chambersburg, PA 17201, USA; thenry@astro.gsu.edu

¹⁰ NASA Ames Research Center, Moffett Field, CA 94035, USA; steve.b.howell@nasa.gov, nic.scott9@gmail.com, rachel.a.matson@nasa.gov

¹¹ Carnegie Observatories, 813 Santa Barbara Street, Pasadena, CA 91101, USA; jteske@carnegiescience.edu

¹² Kavli Institute for Particle Astrophysics and Cosmology, Stanford University, Stanford, CA 94305, USA; lahirsch@stanford.edu

¹³ Department of Earth Sciences, University of California, Riverside, CA 92521, USA; skane@ucr.edu

Received 2018 October 19; revised 2018 December 2; accepted 2018 December 12; published 2019 January 18

Abstract

We present 248 speckle observations of 43 binary and 19 trinary star systems chosen to make progress in two main areas of investigation: the fundamental properties of metal-poor stars and star formation mechanisms. The observations were taken at the Gemini North and South telescopes during the period 2015 July to 2018 April, mainly with the Differential Speckle Survey Instrument but also with a few early results from the new ‘Alopeke speckle camera at Gemini North. We find that the astrometry and photometry of these observations as a whole are consistent with previous work at Gemini. We present five new visual orbits for systems important in understanding metal-poor stars, three of which have orbital periods of less than 4 yr, and we indicate the degree to which these and future observations can impact our knowledge of stellar properties and star formation. In particular, we find a decrease in mass at fixed spectral type for metal-poor stars versus their solar-metallicity analogs that is consistent with predictions that are made from current stellar models.

Key words: binaries: visual – stars: individual – techniques: high angular resolution – techniques: interferometric – techniques: photometric

Supporting material: machine-readable table

1. Introduction

Visual and interferometric binary stars have traditionally been used as tools in two main ways in astronomy: (1) to gain insight into the relationship between fundamental stellar parameters such as mass, radius, luminosity, effective temperature, and metallicity and (2) to provide orbital statistics that are sufficiently robust to distinguish between predictions of star formation theory. Speckle imaging has played a key role in both areas over the last four decades because it offers diffraction-limited resolution in the visible spectrum and is a very efficient, high-precision technique. Many observations can be taken per night, and the quality of those observations can be very high, particularly with regard to the astrometric precision,

which is of great importance for determining orbital elements with which to do astrophysics in either of these lines of investigation.

In recent years, the landscape for speckle imaging has changed significantly. Much better detectors are now available in the form of electron-multiplying CCD cameras, which allow not only for fainter sources to be successfully observed but also for fainter companions to be detected near a primary star of a given magnitude. This realization has paved the way for using the Differential Speckle Survey Instrument (DSSI; Horch et al. 2009) at Gemini for both stellar astrophysics and exoplanet science. Our previous work at Gemini (e.g., Horch et al. 2012) demonstrated the ability to see companions approximately 5 mag fainter than the primary at a separation of 0".1 under typical observing conditions. Another important development is the release of parallax measures from the *Gaia* satellite. Many of the most important “speckle” binaries are small-separation systems, less than 0".2. While for systems resolved by *Gaia*, the parallax measures in the second data release (DR2; *Gaia* Collaboration 2018) are now often much more precise than the *Hipparcos* results (ESA 1997; van Leeuwen 2007), the parallaxes of unresolved binaries can be

¹⁴ Visiting Astronomer, Gemini Observatory, which is operated by the Association of Universities for Research in Astronomy, Inc., under a cooperative agreement with the NSF on behalf of the Gemini partnership: the National Science Foundation (United States), National Research Council (Canada), CONICYT (Chile), Ministerio de Ciencia, Tecnología e Innovación Productiva (Argentina), and Ministério da Ciência, Tecnologia e Inovação (Brazil).

¹⁵ Adjunct Astronomer, Lowell Observatory, 1400 West Mars Hill Road, Flagstaff, AZ 86001, USA.

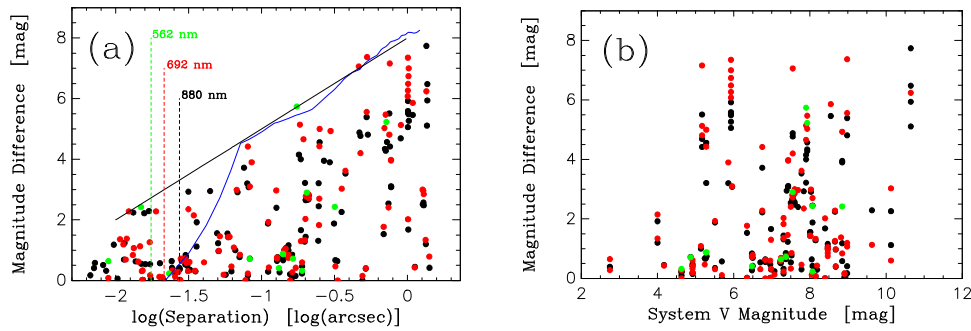


Figure 1. Magnitude difference vs. (a) separation and (b) system *V* magnitude for the measures appearing in Table 2. The colors of the plot symbols indicate the center wavelength of the filter used for the measure, with green indicating 562 nm, red indicating 692 nm, and black used for both 832 and 880 nm. The blue curve in (a) represents a typical detection limit curve for speckle observations at Gemini, which is measured from the noise properties of the reconstructed image and assumes no sensitivity to companions below the diffraction limit. The black line extends the measured sensitivity to the sub-diffraction-limited regime. The dashed vertical lines indicate the location of the diffraction limit for the wavelengths indicated.

affected by the motion of the photocenter of the system and are often not as impressive. It is expected that this will be corrected in DR4, but as it stands, even the results in DR2 provide an instant improvement in the physical separation and mass information that can be gained using resolved binary star images for many systems.

We initiated two observing programs highlighting aspects of binary star science at Gemini soon after DSSI was given visiting instrument status there in 2012. These were focused on the orbits of metal-poor binary stars and the occurrence rate of triple stars in nearby systems as a test of star formation mechanisms. The first results of both programs were published in recent years (Horch et al. 2015a; Tokovinin & Horch 2016), and the current work extends those results in both areas. However, it is interesting to note that as these programs have continued, they have begun to intertwine. Given the sensitivity to large-magnitude difference pairs at Gemini with DSSI, a number of the metal-poor objects have been found to have faint third companions. The recent work of Moe et al. (submitted 2018) suggests an anticorrelation between close ($P < 10^4$ days) binary fraction and metallicity, as well as an increase in wide triples at lower metallicities, so our small sample may in fact simply mirror their result if it proves to be true. In terms of the trinary program, sustained observations of the small-separation pairs in these systems can lead to high-precision orbits, aiding our knowledge of stellar masses for a range of metallicity. Given this, we detail here the latest results of both programs together and report the discovery of 12 previously unknown or unresolved components.

2. Observations and Data Reduction

The observations described here were taken at the Gemini North and South telescopes over the period of 2015 July through 2018 April. Results from seven different observing runs have been combined, including two in which the new ‘Alopec’ speckle camera (Scott et al. 2016; N. J. Scott et al. 2018, in preparation) was used at Gemini North. However, in total, the observations here represent the use of only about 3 nights of telescope time, including all calibrations. (Several other approved programs also used DSSI while it was on the telescope.) This highlights the fact that significant progress can be made on these science goals with a modest investment of observing time, provided that the time is consistently scheduled over a period of years. Figure 1 shows the basic properties of the sample of observations presented here; in panel (a), the

magnitude differences are plotted against the separations determined for these systems. Secondary stars as faint as 6 mag fainter than the primary are able to be successfully observed and measured at separations as close as $0''.2$. In Figure 1(b), the same magnitude differences are plotted versus the system *V* magnitudes. The sample is bright ($V = 2\text{--}11$) and nearby (median distance = 56 pc), and Gemini’s large aperture enables the resolution and measurement of extremely small-separation systems. In Figure 1(a), a typical 5σ contrast curve is shown from our previous work at Gemini with DSSI; the fact that the measurements here fill this parameter space indicates that our detection capabilities are similar to our previous observations. A number of points appear above the curve at extremely small separations, and in fact, most of these are below the formal diffraction limit; in these cases, we have measured the binary parameters using the techniques described in Horch et al. (2006) for DSSI data. These systems remain blended in the final reconstructed images that we derive from the speckle data, but nonetheless, we find strong agreement in the derived position angles and separations in the two filters used. In many cases, these are known to be binary from previous spectroscopic observations as well.

2.1. Reduction Method

The reduction method used here is the same as has been detailed in our recent papers (Horch et al. 2012, 2015a, 2015b; Tokovinin & Horch 2016). A reconstructed image is made from the raw data using the technique of bispectral analysis (Lohmann et al. 1983), and phase retrieval in the Fourier domain is performed with the relaxation algorithm of Meng et al. (1990). The reconstructed image in each filter is used to identify the components of the system. Once the position of a component has been noted to the nearest pixel, a downhill simplex algorithm is used to fit the power spectrum of the science target to a cosine squared function in the Fourier plane. The spacing, orientation, and depth of the fitted fringes are then converted into a separation, position angle, and magnitude difference for the system. Before fitting the power spectrum, the science observation must be deconvolved with the power spectrum of a point source. For most of the observations here, the point source used was taken at low zenith distance, and then a dispersion model was applied that included the altitude and azimuth of the science target at the time of observation to derive the power spectrum that was used in the deconvolution. This makes the point source the best possible match for the

Table 1
Orbits Used in the Scale Determinations

Run	Telescope	Instrument	WDS	Discoverer Designation	HIP	Orbit Reference
2015 Jul	Gemini-N	DSSI	17080+3556	HU 1176AB	83838	Muterspaugh et al. (2010)
			21145+1000	STT 535AB	104858	Muterspaugh et al. (2008)
2016 Jan	Gemini-N	DSSI	04136+0743	A 1938	19719	Muterspaugh et al. (2010)
			22409+1433	HO 296AB	111974	Muterspaugh et al. (2010)
2016 Jun	Gemini-S	DSSI	18384−0312	A 88AB	91394	Griffin (2013)
			19026−2953	HDO 150AB	93506	DeRosa et al. (2012)
2017 Jun	Gemini-S	DSSI	18384−0312	A 88AB	91394	Griffin (2013)
			19026−2953	HDO 150AB	93506	DeRosa et al. (2012)
2017 Dec	Gemini-N	'Alopeke	13100+1732	STF 1728AB	64241	Muterspaugh et al. (2015)
			15232+3017	STF 1937AB	75312	Muterspaugh et al. (2010)
			15278+2906	JEF 1	75695	Muterspaugh et al. (2010)
2018 Mar/Apr	Gemini-S	DSSI	06573−3530	I 65	33451	Docobo & Ling (2009)
			07518−1354	BU 101	38382	Tokovinin (2012)
			08270−5242	B 1606	41426	Tokovinin et al. (2015)
			16044−1122	STF 1998AB	78727	Docobo & Ling (2009)
2018 Mar/Apr	Gemini-N	'Alopeke	13100+1732	STF 1728AB	64241	Muterspaugh et al. (2015)
			15232+3017	STF 1937AB	75312	Muterspaugh et al. (2010)
			15278+2906	JEF 1	75695	Muterspaugh et al. (2010)

dispersion that exists in the science data. For the remainder of the targets, especially the 'Alopeke observations, a point source was observed near in time and sky position, and this was used for the deconvolution.

In the case of triple stars, the reduction follows along the same lines, except that once the reconstruction is calculated, the rough positions of both components are noted. These are used to generate a trial power spectrum that exhibits two sets of superimposed fringes, and this is compared with the (deconvolved) power spectrum of the data. Then, the downhill simplex method is used to minimize the weighted least-squares result between the data and fit, which in turn yields a final position angle, separation, and magnitude difference value for both of the companion stars.

2.2. Pixel Scale and Orientation

The standard method for measuring scale and orientation in speckle imaging is to mount a slit mask on the telescope and observe a bright single star. The slits create fringes on the image plane, which allow the scale to be measured from first principles, if the wavelength band of the observation is narrow and the color of the target star is known. At Gemini, it has not been possible to mount a slit mask for speckle observations to date, so we instead use a small collection of calibration binaries—that is, binaries with extremely well-known orbits—often determined with a large weighting of data points derived from long-baseline optical interferometry observations. Table 1 shows the systems used during our Gemini runs for this purpose and the references for the orbits used to calculate ephemeris positions for the epoch of observations in our case, where the ephemeris separations ranged from 0.1 to 1''1. It has been several years since the orbit calculation in a number of those cases, so we also studied the recent observations listed in the Fourth Interferometric Catalog of Measurements of Binary Stars (4th Interferometric Catalog; Hartkopf et al. 2001b) to identify any current trends in the residuals versus the orbital ephemerides. Where they were found, they were incorporated into the final scale determination for the run by adding the mean residual onto the ephemeris value prior to determining a scale value. The final scale was then a weighted average

between this value and that obtained when no residuals were incorporated, with the weighting determined by how clearly the residuals showed that the system was deviating from the orbit prediction. A similar procedure was followed for determining the position angle offset, and our calculations also included the known distortion in the reflective channel of DSSI, most recently discussed in Horch et al. (2017).

In comparing the scales and orientations derived for the runs shown in Table 1, the basic pattern that we have seen at other telescopes emerged here as well, namely that the scale values fluctuate by as much as 1% from run to run, and the offset angle relative to the celestial coordinates also varies by over 1°. As a consequence, and given that we are combining data from two different telescopes and two different instruments, we judge that the most conservative approach is to treat each run independently in terms of the scale determination. However, this comes at a cost: it leaves us with only two or three objects with which to determine the scale for each run, and therefore the uncertainties in the scale are larger than one would ideally like for precision astrometry. Once the scale and orientation values have been fixed for each run, we can compute the average residuals obtained on our scale objects using ephemeris predictions (that is, not including the trends in residuals of other recent observations discussed above), and we find that the standard error in the scale determined for each run, when averaged over all runs, is $0.43\% \pm 0.12\%$. For the orientation angle, the result was $0^\circ.41 \pm 0^\circ.11$. This topic will be discussed further in Section 3.2, where comparisons with other known positions of some of our objects are made.

Looking toward the future, we are actively considering how to devise the most precise means for determining pixel scale and orientation. For example, when faced with a similar problem, Tokovinin et al. (2010) used two coherent light sources mounted at a fixed distance on the telescope spider to create fringes on the image plane; this is one possibility. However, the new Gemini speckle cameras, 'Alopeke (already commissioned at Gemini North) and Zorro (expected to be commissioned in 2019 at Gemini South), also have the ability to mount an aperture mask inside the instrument in the collimated beam. This is the most likely long-term solution to the pixel scale issue for precise astrometry.

Table 2
Binary Star Speckle Measures

WDS (α , δ J2000.0)	HR, ADS, DM, etc.	Discoverer Designation	HIP	Date (2000+)	θ (deg)	ρ (arcsec)	Δm (mag)	λ (nm)	$\Delta\lambda$ (nm)
1	2	3	4	5	6	7	8	9	10
01011+1622	BD+15 150	DSG 9	4754	16.0338	36.0	1.3607	<5.11 ^a	880	50
				16.0420	34.0	1.3479	<6.24 ^a	692	40
				16.0420	35.8	1.3484	<7.74 ^a	880	50
				16.0448	35.0	1.3678	<5.94 ^a	880	50
				17.9476	38.0	1.3679	<6.48 ^a	832	40
01057+2128	ADS 899	YR 6Aa, Ab	5131	17.9476	311.8	0.1404	0.87	562	44
				17.9476	312.0	0.1405	0.67	832	40
01083+5455	HD 6582	WCK 1Aa, Ab	5336	15.5448	34.5	0.9018	5.13	692	40
				15.5448	32.0	0.8991	4.69	880	50
				16.0337	30.9	0.7560	7.16	692	40
				16.0337	31.0	0.7510	5.51	880	50
				16.0474	30.6	0.7513	4.81	692	40
				16.0474	27.7	0.7589	4.42	880	50

Note.

^a The photometry for this observation appears as an upper limit because the observation may be affected by speckle decorrelation, as discussed in the text.

^b Quadrant inconsistent with previous measures in the 4th Interferometric Catalog (Hartkopf et al. 2001b).

^c A magnitude difference for this single-lined spectroscopic binary does not appear for the reasons discussed in the text for small-separation systems.

^d The position angle of this observation was found to be in the opposite quadrant from that of the observation in the other filter. To keep the position angles consistent, we adopt a negative magnitude difference for this observation.

^e The component was undetected in this filter, with a lower limit in the magnitude difference shown.

(This table is available in its entirety in machine-readable form.)

3. Results

Table 2 shows the main results of our observations. The columns are (1) the Washington Double Star (WDS) number (Mason et al. 2001), which also gives the R.A. and decl. for the object in 2000.0 coordinates; (2) a secondary identifier, most often the Henry Draper Catalog (HD) number for the object; (3) the discoverer designation; (4) the *Hipparcos* Catalog number (ESA 1997); (5) the Besselian date of the observation (minus 2000)¹⁶; (6) the position angle (θ) of the secondary star relative to the primary, with north (0°) through east (90°) defining the positive sense of θ ; (7) the separation of the two stars (ρ) in arcseconds; (8) the magnitude difference (Δm) of the pair in the filter used; (9) the center wavelength of the filter used; and (10) the full width at half maximum of the filter transmission in nanometers. Position angles have not been precessed from the dates shown and are left as determined by our analysis procedure, even if inconsistent with previous measures in the literature. (However, wherever possible, we have noted these inconsistencies.)

Twelve objects have no previous detection of the companion noted; given that we identified eight doubles in previous papers in this series containing Gemini speckle observations (Horch et al. 2012, 2015a), we suggest discoverer designations of DSG (DSSI-Gemini) 9–20 and will refer to them as such throughout the rest of this paper. It is of course possible that some of these discoveries are line-of-sight companions; this is statistically more likely to be the case for components that have larger separations and magnitude differences, as shown in Horch et al. (2014) and, more recently, Matson et al. (2018).

Figure 2 shows the discovery images for two systems, one new discovery and one triple. In Figures 2(a) and (b), the 692

and 880 nm reconstructed images show a very faint companion detected at a separation of $1''.3$ from the primary star of HIP 4754 = BD+15 150. In Figures 2(c) and (d), we show reconstructed images of HDS 2092, a triple star where we clearly resolve the secondary into a small-separation pair, recently identified by Tokovinin et al. (2018).

3.1. Comments on Newly Resolved Pairs

Some further brief commentary on the 12 stars that host the previously unknown companions is given below. The basic observational data discussed for each system are taken from SIMBAD,¹⁷ the Ninth Catalog of Spectroscopic Orbits of Binary Stars (9th Spectroscopic Catalog; Pourbaix et al. 2004), and the Geneva–Copenhagen spectroscopic survey (Holmberg et al. 2009).

1. DSG 9 (HIP 4754). This F7 subdwarf is probably a triple system; the faint component seen in our observations is much too large a separation to correspond to the spectroscopic system that has a period of 347 days, as determined by Latham et al. (2002). In that same work, the authors determined the metal abundance to be $[\text{Fe}/\text{H}] = -1.5$. (This system is shown in Figure 2.)
2. DSG 10 (HIP 19915). In the Geneva–Copenhagen spectroscopic survey, this system was found to have a metal abundance $[\text{Fe}/\text{H}]$ of -2.01 , and it was also noted as a double-lined spectroscopic binary with a mass ratio of 0.904 ± 0.019 . We see not only what is most likely the spectroscopic component and previously given discoverer designation, YSC 129, but also a faint, wide component at a separation of half an $0''.5$. This system could play an important role in our understanding of the fundamental properties of true Population II stars if

¹⁶ If Julian Dates are preferred, the conversion formula between Besselian year and Modified Julian Date is found at <https://www.usno.navy.mil/USNO/earth-orientation/eo-info/general/date-time-def>.

¹⁷ <http://simbad.u-strasbg.fr/simbad/>

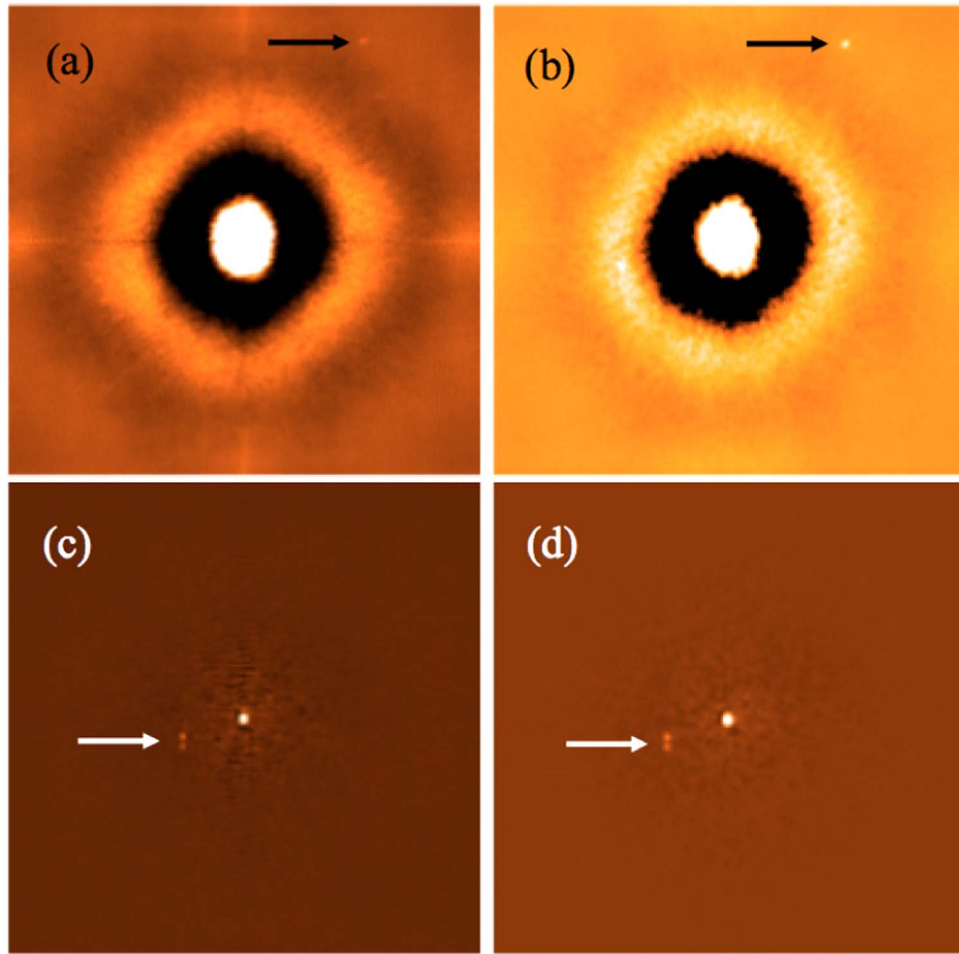


Figure 2. Reconstructed images of two systems presented in Table 2. (a) DSG 9 = HIP 4754 at 692 nm. (b) DSG 9 at 880 nm. A very faint, previously unknown companion (shown with the arrow in each image) was detected with this known spectroscopic binary star (which is unresolved here). The apparent very faint peak to the left and slightly below the primary in the 880 nm image is a known reflection in the instrument. (c) Triple system HD 2092 = HIP 72492 at 692 nm. (d) HDS 2092 at 880 nm. In this case, the secondary of the known binary HDS 2092 was resolved into a small-separation pair. In all cases, north is up and east is to the right. Each image is 2.8×2.8 arcsec in size.

further observations can be obtained and the orbital motion studied.

3. DSG 11 (HIP 34105, HR 2683). This variable A star was originally selected as a point-source calibration object for one of the science targets in our program. The *Gaia* DR2 parallax puts the distance to the system at approximately 86 pc, leading to a projected separation of 5 au for the binary at present, if the pair is gravitationally bound.
4. DSG 12 (HIP 56851). This system was listed as a double-lined spectroscopic binary in the Geneva–Copenhagen survey, with a mass ratio of 0.983. The component in Table 2, however, has a magnitude difference of over 2. Given the parallax of 6.8384 ± 0.0358 mas and our separation of $0''.03$, a projected separation of 4.4 au is obtained for this late-G, metal-poor subgiant. Thus, it is likely to be a triple system.
5. DSG 13 (HIP 57421). Our observations confirm that there are two companions within $0''.5$ of this previously known speckle double, but it is not an obviously hierarchical system. It is also known to be a double-lined binary of near equal masses, but with projected separations of tens of au for both of the resolved components (if bound), neither is likely to be the spectroscopic component. Given a large proper motion for the primary

star ($\mu_x = -85.951$ mas), it should be straightforward to establish if one or both of these components is a line-of-sight companion in the coming years, if further observations are obtained.

6. DSG 14 (HIP 58669). There are double-lined spectroscopic orbits for both the small- and large-separation pairs in this triple system (Tokovinin et al. 2015). We resolve the small-separation component for the first time (the wider pair being WDS 12018–3439 = I 215). The primary star is a solar near-twin, with the same metal abundance and early-G spectral type.
7. DSG 15 (HIP 61158, HR 4771). The small-separation component to this bright, late-A giant is approximately 3 mag fainter than the primary and less than $0''.1$ away, illustrating the power of speckle imaging at Gemini. Virtually no difference in color between the two stars is noted, so the secondary may be a late-A dwarf.
8. DSG 16Aa, Ab (HIP 68587). We detect here a very small-separation companion to the brighter star in the known pair B 263. The primary would appear to be a near-solar analog, with $[\text{Fe}/\text{H}]$ of -0.02 and spectral type G3V.
9. DSG 17 (HIP 72622, HR 5531). Although there is no indication of duplicity for this star in the literature, we

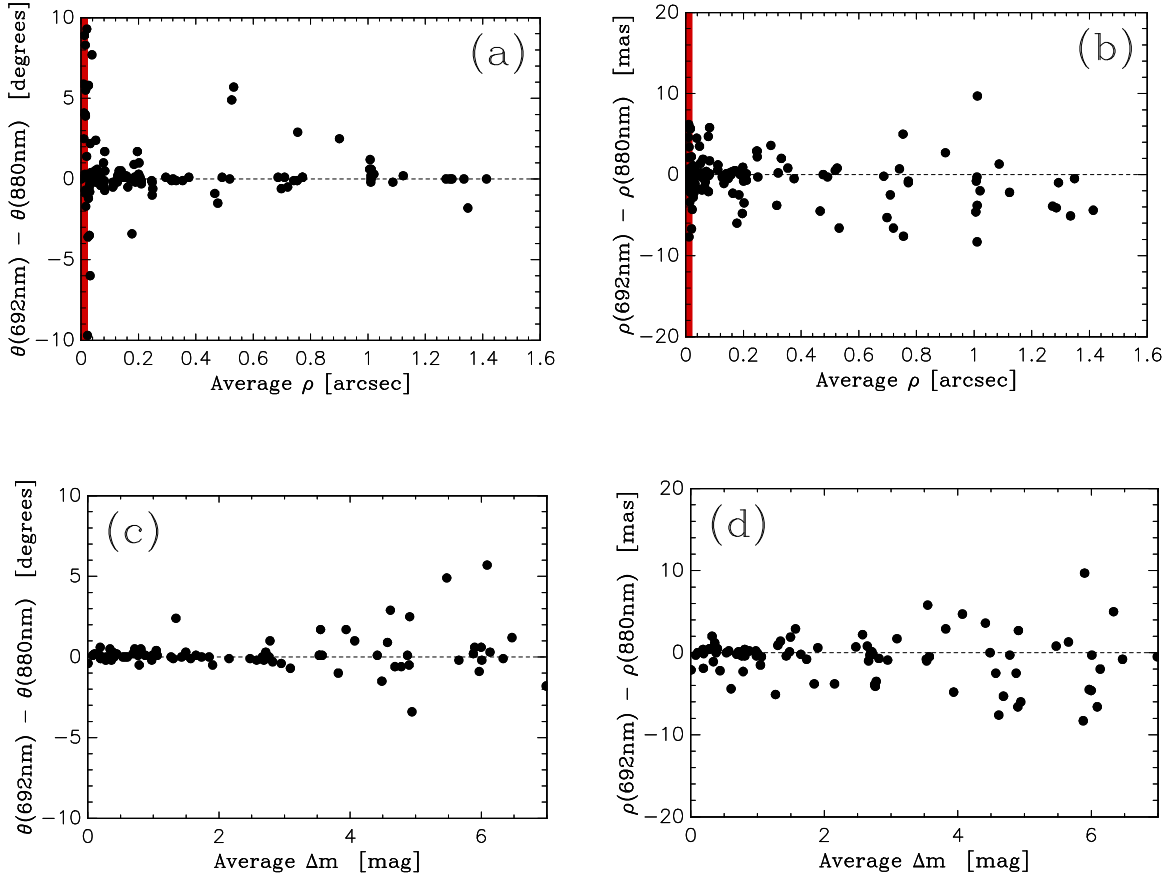


Figure 3. Measurement differences between the two channels of the instrument for position angle and separation plotted as functions of measured separation ρ in (a) and (b) and as functions of Δm in (c) and (d). In (a) and (b), the dark red band at the left marks the region below the diffraction limit of the telescope, and in all plots, a dotted line is drawn at zero to indicate perfect agreement between the channels.

find a small-separation companion to this nearby mid-A subgiant. Within a few years, orbital motion should be apparent if the system is gravitationally bound.

10. DSG 18 (HIP 76424, HR 5804). This star lies 52 pc from the solar system, but the component we find is at a separation of $1''$. Thus, if physically bound to the F3V primary star, the orbital period of the secondary is likely to be in the range of hundreds of yr.
11. DSG 19 (HIP 80925). This system has a single-lined spectroscopic orbit in the 9th Spectroscopic Catalog due to Bopp et al. (1970), but it more recently appeared in the list of double-lined systems for which Holmberg et al. (2009) gave a mass ratio; they obtained a value of 0.919 ± 0.020 . They also measured the metal abundance as $[\text{Fe}/\text{H}] = -0.60$ for this K1V star. A component with an $\sim 4''$ separation was discovered by *Hipparcos* (HDS 2335), but that would not be present in the small ($2.8 \times 2.8''$) field of view for DSSI at Gemini, and in any case, it has a much larger magnitude difference than what we detect here. We conclude that the component detected here is the spectroscopic one, particularly given that the system is only 22 pc from the solar system, and the projected separation is therefore approximately 0.2 au.
12. DSG 20 (HIP 81170). We measure the separation of this known double-lined spectroscopic binary for the first time. The system is very metal-poor, with $[\text{Fe}/\text{H}] = -1.39$, but relatively nearby, at a distance of 43 pc. If further observations can be obtained in the future at

Gemini, the possibility of a spectroscopic-visual orbit exists within the next few years, and the system could give information relevant to studies of low-metallicity stars, as discussed in Section 4.2.

3.2. Relative Astrometry and Photometry

We can judge the precision of our astrometric results by examining the differences in position angles and separations obtained on the same observations in the two different filters used. These are shown in Figure 3 in two ways. In panels (a) and (b), these differences are plotted as a function of average measured separation. As expected, they show that at smaller separations, the position angle precision deteriorates, although the scatter remains fairly symmetric about zero, indicating no systematic offsets between the two channels of the instrument. On the other hand, the scatter of the separation differences remains fairly constant with separation (again with a near-zero mean). In panels (c) and (d), the same differences are plotted as a function of the measured magnitude difference, whereupon it is clear that in both position angle and separation, the scatter grows as the magnitude differences increase. Overall, for the complete sample, the mean difference is -0.44 ± 0.27 mas in separation and $+1^{\circ}19' \pm 0^{\circ}49'$ in position angle; however, if separations are confined to the range $0''.05$ – $1''.0$, then these numbers become -0.37 ± 0.30 mas in separation and $0^{\circ}25' \pm 0^{\circ}14'$ in position angle. The standard deviation of the residuals in the former case is 2.54 ± 0.21 mas for separation

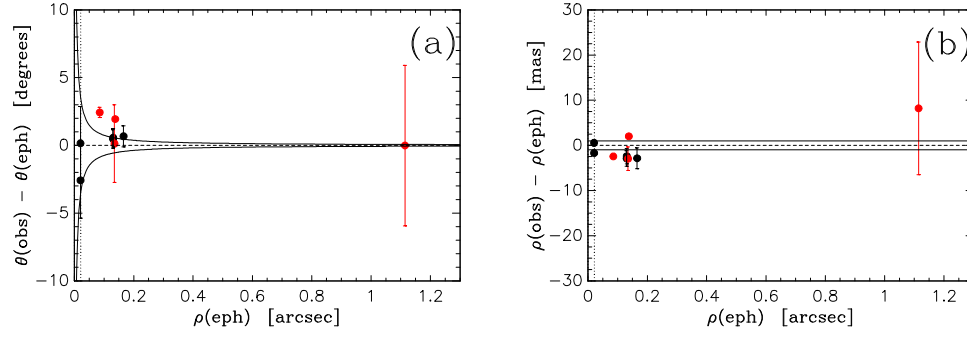


Figure 4. (a) Position angle residuals for measures in Table 2 when comparing to orbits of Grade 1 or 2 in the 6th Orbit Catalog (Hartkopf et al. 2001a). (b) Separation residuals for the same observations. Red data points indicate Grade 1 orbits, and black data points are used for Grade 2 orbits. A dashed horizontal line is drawn to indicate the zero residual line, and in panel (a), a 1.3 mas uncertainty is used to create the solid curves to indicate how that uncertainty translates into a position angle uncertainty. In panel (b), solid lines are drawn at ± 1.3 mas to indicate the uncertainty of our speckle measures. The vertical dotted lines mark the diffraction limit of the telescope at 692 nm.

Table 3
Ephemeris Positions and Residuals Used in the Astrometric Accuracy Study

WDS	Discoverer Designation	HIP	Date (2000+)	θ_{eph} (deg)	ρ_{eph} (arcsec)	$\Delta\bar{\theta}$ (deg)	$\Delta\bar{\rho}$ (mas)	WDS Orbit Grade and Reference
1	2	3	4	5	6	7	8	9
02396–152	FIN 312	12390	17.9477	200.9 ± 0.4	0.0855 ± 0.0004	+2.4	–2.5	1; Docobo & Andrade (2013)
04107–0452	A 2801	19508	16.0368	345.7 ± 0.7	0.1304 ± 0.0017	+0.5	–2.9	2; Tokovinin (2017)
			16.0476	345.8 ± 0.7	0.1307 ± 0.0017	+0.6	–2.1	
			18.2460	355.0 ± 0.8	0.1658 ± 0.0023	+0.7	–2.9	
04136+0743	A 1938	19719	17.9477	328.1 ± 0.1	0.1377 ± 0.0002	+1.9	+2.0	1; Muterspaugh et al. (2010)
16044–122	STF 1998	78727	18.2490	9.0 ± 5.9	1.1145 ± 0.0147	–0.0	+8.2	1; Docobo & Ling (2009)
18099+0307	YSC 132Aa, Ab	89000	15.5277	149.6 ± 2.7	0.0206 ± 0.0006	+0.1	+0.6	2; Méndez et al. (2017)
			18.2525	152.9 ± 2.8	0.0207 ± 0.0006	–2.6	–1.7	
18384–0312	A 88AB	91394	16.4880	193.4 ± 2.9	0.1351 ± 0.0026	+0.1	–3.0	1; Griffin (2013)

and $1^{\circ}21 \pm 0^{\circ}10$ for position angle. These numbers imply that for an individual measure (not a difference between two measures of the same uncertainty, as these numbers represent), the precision would be estimated as the standard deviation divided by $\sqrt{2}$, so that, on average, the uncertainties in the position angle and separation values given in Table 2 are 1.8 mas and $0^{\circ}9$, respectively. A further improvement could be obtained if the measures in each channel were averaged; in that case, the uncertainties would be reduced by another factor of $\sqrt{2}$, resulting in 1.3 mas and $0^{\circ}6$. These numbers are very close to those of our previous studies involving Gemini DSSI data (e.g., 0.9 mas and $1^{\circ}0$ were obtained in Horch et al. 2015a for a data set with fewer large-magnitude difference systems and generally smaller separations).

Below the diffraction limit, the measurement uncertainty increases. For example, the collection of measures with separations below 22 mas (the diffraction limit for the 692 nm filter) in Table 2 has a standard deviation of separation differences between the two channels of 3.53 ± 0.54 mas, approximately 40% higher than the result for all observations with separations between $0^{\circ}05$ and $1''$. Assuming that the linear measurement uncertainty is the same in the direction along the position angle coordinate as in the radial direction, the uncertainty in position angle should be related to the separation and uncertainty in separation by

$$\delta\theta = \arctan\left[\frac{\delta\rho}{\rho}\right]. \quad (1)$$

For the separations below the diffraction limit at Gemini, $\delta\theta$ increases substantially due to the combined effects of the

dependence on ρ and the larger value of $\delta\rho$ itself, indicating that larger differences in position angle between the two channels will be seen in this separation regime. For the measures below 22 mas, we find the standard deviation in position angle differences to be $11^{\circ}6 \pm 1^{\circ}8$, which is roughly consistent with the application of the above formula using $\delta\rho = 3.53$ mas and the average separation for the measures in question, 14.1 mas. In that case, the value we obtain is $14^{\circ}1$.

In Figure 4, we investigate the accuracy of the measures, as judged by comparisons with the ephemeris predictions for systems with well-known orbits (excluding, of course, systems that were used in the determination of the scale and orientation). We confine our comparison to those systems with either Grade 1 or Grade 2 orbits in the Sixth Catalog of Visual Orbits of Binary Stars (6th Orbit Catalog; Hartkopf et al. 2001a). We further impose the criterion that the orbit used must list uncertainties to the orbital elements, so that we can propagate those uncertainties into the predicted separation and position angle for the epoch in which we observed the star. Ephemeris positions and residuals for these objects are shown in Table 3, where the astrometry from both channels of DSSI has been averaged before making the comparison. The columns give (1)–(3) the WDS, discoverer designation, and *Hipparcos* number; (4) the date of the observation; (5) and (6) the position angle and separation derived from the orbital elements for the date in question; (7) and (8) the residuals in each coordinate when comparing to the values in Table 2; and (9) the orbit grade and reference. The table and Figure 4 indicate that, as far as we can tell, there are no systematic differences between our measures and the ephemeris predictions. Formally, the mean

Table 4
A Comparison of Astrometry from Table 2 with *Gaia* DR2 Results

WDS	Discoverer Designation	HIP	Date (2000+)	θ_{Gaia} (deg)	ρ_{Gaia} (arcsec)	$\Delta\bar{\theta}$ (deg)	$\Delta\bar{\rho}$ (mas)
1	2	3	4	5	6	7	8
16120–1928	BU 120Aa-B	79374	17.4298	2.4	1.3263	−1.4	+8.0
17066+0039	BU 823A, Ba	83716	17.4327	173.6	0.9901	−3.8	+20.6
18093–2607	HDS 2560Aa, Ab	88937	16.4662	340.2	1.2988	+1.8	−6.1
		88937	17.4301	340.2	1.2988	+2.1	−13.8
		88937	18.2464	340.2	1.2988	+3.0	−26.7
18112–1951	BU 132Aa, B	89114	17.4328	184.5	1.4051	+2.1	+8.1

residual is -0.50 ± 1.23 mas in separation and $0^\circ.42 \pm 0^\circ.47$ in position angle.

A final astrometric check was done using four objects with separations above $1''$ in Table 2 that appear as resolved objects in the *Gaia* DR2. From the *Gaia* positions, we deduce the position angle and relative separations of each pair and form the difference in each quantity relative to the values in Table 2. The results are shown in Table 4, where the columns give (1) the WDS designation, (2) the discoverer designation, (3) the *Hipparcos* number, (4) the date of our observation, (5) and (6) the position angle and separation of the pair derived from positions in DR2, and (7) and (8) the (speckle minus *Gaia*) difference in these quantities. As in Table 3, we have averaged the results in the two filters shown in Table 2 before using the astrometry in Table 4. For the ensemble of measures on these four objects, the mean residual in separation is -1.6 ± 4.8 mas, and in position angle, we obtain $+0^\circ.63 \pm 1^\circ.08$, indicating no evidence of scale or orientation offsets. The scatter is larger than the differences between channels and orbit residuals discussed above, but that can be explained by a small amount of relative motion of these pairs in between our measures and those of *Gaia*, which were not taken at the same epoch. In addition, three of the four systems are triple stars, where the small-separation component is not seen in DR2 but is resolved in our observation, thus potentially affecting the astrometry.

The absolute value of the mean residual in separation divided by the average separation of the sample yields a value of $0.23\% \pm 0.57\%$ for the orbit study and $0.13\% \pm 0.38\%$ for the *Gaia* comparison. If we assume that this represents the implied scale offset, then both numbers are somewhat smaller than (but certainly consistent with) the number quoted for the scale uncertainty in Section 2.2. The position angle residuals in both studies are likewise similar to the number given for the position angle uncertainty. Therefore, we conclude that the values given in Section 2.2 are reasonable estimates of the contributions to the overall uncertainty in our measures coming from scale and orientation calibration. To obtain the total uncertainty in separation for any measure in Table 2, one would multiply the measure by the scale uncertainty and add that in quadrature with the internal precision estimate of 1.8 mas as follows:

$$\delta\rho = \sqrt{1.8^2 + (\rho \cdot 0.0043)^2}, \quad (2)$$

where ρ is the observed separation in mas. This yields, for example, $\delta\rho = 1.8$ mas for $\rho = 0.1$ arcsec, 2.7 mas for $0''.5$, and 4.4 mas for $1''.0$. The total uncertainty in position angle would be obtained by adding the internal precision and the

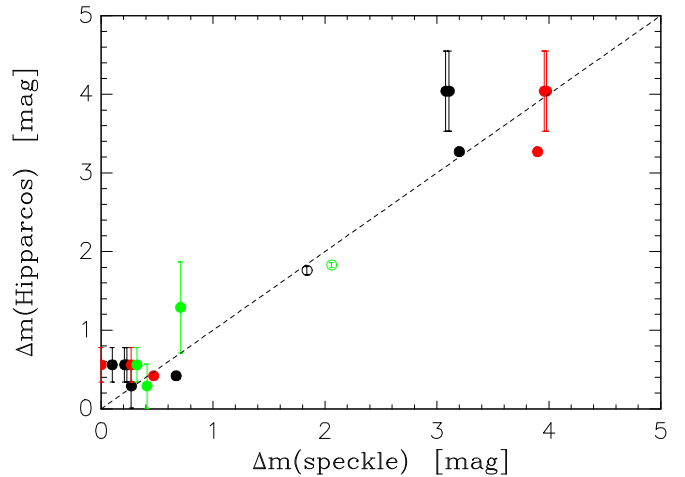


Figure 5. Measures of magnitude difference obtained in the analysis here vs. those appearing in the *Hipparcos* Catalog (using the H_r filter). The open circles are the result for HIP 75695 = JEF 1, where there is no *Hipparcos* measure but there are several recent measures from our work at WIYN and the DCT, so those are used for the comparison here. The color of the plot symbol indicates the filter of the speckle observation: green represents 562 nm, red represents 692 nm, and black represents 832 or 880 nm.

offset uncertainty in quadrature; that results in a value of $\sqrt{0.9^2 + 0.4^2} = 1^\circ.0$.

Turning now to the relative photometry, we have studied the magnitude differences derived from our observations together with the *Hipparcos* values in the few cases where relative photometry exists in the *Hipparcos* Catalog (ESA 1997). A comparison is shown in Figure 5, where the relationship between the space-based values and those here appears to be linear to the extent that we can judge. All of our observations that are relevant, regardless of the filter used, are plotted in the figure. While it is hard to conclude much from so few points, and the comparison itself is rough due to the difference in center wavelength of the filters being compared, we can observe that the scatter of the points appears to be roughly in line with previous studies using DSSI (Horch et al. 2012, 2015a). It is known from our previous work that the uncertainties in magnitude difference grow below $\Delta m = 0.5$ and above $\Delta m = 3.0$ (Horch et al. 2004); for data reported here in the range of $0.5 \leq \Delta m \leq 3$, we obtain a standard deviation in the Δm residual of 0.16 ± 0.07 for the three highest-precision *Hipparcos* values. This includes the canonical uncertainty in Δm that we have stated in other papers of about 0.1 mag for most observations under good observing conditions.

In other papers in this series (e.g., Horch et al. 2015b), we have discussed how seeing and the separation of a binary

Table 5
Orbital Elements for Five Systems

Parameter	WCK 1Aa, Ab	YSC 129	LSC 45	DSG 7Aa, Ab	DSG 8
HIP	5336	32040	36387	81023	117415
Sp. orbit type	SB1	SB2	none	SB1	SB2
P , yr	21.479 ± 0.032	2.5594 ± 0.0035	40.8 ± 2.6	0.61867 ± 0.00033	3.2191 ± 0.0038
a , mas	989.8 ± 5.4	33.7 ± 0.7	95.3 ± 3.3	16.0 ± 1.2	40.8 ± 1.0
i , deg	111.40 ± 0.27	105.2 ± 2.5	59.2 ± 1.0	117.9 ± 8.2	86.0 ± 0.9
Ω , deg	41.28 ± 0.63	280.7 ± 1.4	24.6 ± 63.6	162.7 ± 8.2	121.1 ± 1.1
T_0 , yr	1975.5514 ± 0.0805	2002.7371 ± 0.0155	2011.6 ± 8.0	1988.4316 ± 0.0030	2011.0545 ± 0.0085
e	0.6251 ± 0.0099	0.158 ± 0.007	0.092 ± 0.033	0.3067 ± 0.0088	0.602 ± 0.008
ω , deg	144.93 ± 1.63	296.8 ± 2.3	193.9 ± 34.9	20.46 ± 1.74	78.4 ± 0.6
K_1 (km s $^{-1}$)	2.62 ± 0.11	14.35 ± 0.13	...	23.62 ± 0.23	16.41 ± 0.18
K_2 (km s $^{-1}$)	...	15.07 ± 0.13	16.24 ± 0.22
v_0 (km s $^{-1}$)	-97.560 ± 0.063	82.65 ± 0.07	...	-51.28 ± 0.15	-9.50 ± 0.07

system affect the relative photometry because they determine the degree to which the speckle pattern of the secondary star is within the isoplanatic patch. However, in the present case, due to the combination of small separation and excellent seeing, nearly all measures meet the quality criteria we have set forth in the past for reporting magnitude differences. Nonetheless, we have applied the same methodology to the current data set, and in a small number of cases (of separations larger than approximately $1''$), we list the magnitude difference obtained in the fit as an upper limit, to indicate that the observation could be affected by speckle decorrelation.

Another situation that we have studied in some detail since our last publication of Gemini data is that of small-separation, large-magnitude difference systems. In Horch et al. (2015a), we presented observations of the triple system HIP 103987 and derived a visual orbit from the data of the small-separation component that we now believe to be spurious. It has since been superseded by the orbit of Tokovinin & Latham (2017), where those authors warned of possible systematic errors in the determination of our astrometry and photometry of the small-separation pair in this system, DSG 6Aa, Ab. We have reviewed the data reduction of those observations and at this time retract the measures taken at Besselian years 2012.5739 and 2014.5645 as most likely dominated by atmospheric dispersion. On the other hand, our observations made in 2013 and 2015 appear to be on firmer ground, as they were taken at modest zenith angles and in rough agreement with the Tokovinin and Latham orbit. Thus, we cannot retract the 2013 observation on the same basis, but it should be viewed as uncertain in the context of this discussion, and we will not report the only new measure (from 2015) here. We will seek further observations of the system to either confirm or refute its detection.

4. New Orbital Elements

The measures in Table 2, together with those found in the 4th Interferometric Catalog, allow us to give updated visual orbital elements for four spectroscopic binaries and report orbital elements of one system for the first time. These are presented in Table 5. For four of the five systems, namely WCK 1Aa, Ab (WDS 01083+5455, HIP 5336), YSC 129 (WDS 06416+3556, HIP 32040), DSG 7Aa, Ab (WDS 16329+0315, HIP 81023), and DSG 8 (WDS 23485+2539, HIP 117415), a visual-spectroscopic orbit calculation was performed, where radial velocities found in the 9th Spectroscopic Catalog were used. In these cases, the method was that of

Tokovinin (2016). Calculating the orbit of DSG 7Aa, Ab was sufficiently challenging that we averaged the astrometry obtained in the two filters before using that as input for the orbit calculations. This leaves us with only four points to work with in calculating the visual orbital elements, and therefore the orbit obtained here should be viewed as tentative.

In the case of LSC 45 (WDS 07293+1227, HIP 36387), a preliminary orbit is determined using the visual orbit code of MacKnight & Horch (2004), which starts with a grid search over a user-specified range of each parameter and then uses a downhill simplex algorithm to arrive at final parameters that minimize the reduced χ^2 of the least-squares fit. In the orbit computed here, Gemini points were given twice as high a weight as any points derived from 4 m class telescopes, as the astrometry at Gemini is more precise. Visual representations of all five orbits calculated here are shown in Figure 6.

4.1. Further Comments on the Individual Systems

4.1.1. μ Cas = WCK 1Aa, Ab = WDS 01083+5455

We update the visual orbit of Drummond et al. (1995) for this system with visual-spectroscopic orbital elements for this well-known single-lined spectroscopic binary. It is a somewhat metal-poor system ($[\text{Fe}/\text{H}] = -0.68$; Boyajian et al. 2008) with a composite spectral type of G5V. Both the period and semimajor axis are slightly decreased from the Drummond et al. values, leading to a lower total mass estimate by a few percent. The *Gaia* DR2 does not list a parallax for this system, but fortunately, the revised *Hipparcos* result (van Leeuwen 2007) is precise to better than 1%: 132.38 ± 0.82 mas. From this, we determine that $M_{\text{tot}} = 0.906 \pm 0.023 M_{\odot}$.

4.1.2. YSC 129 = WDS 06416+3556

This system, with period of 2.57 yr, was first resolved at the WIYN telescope in 2010 as a part of the Yale–Southern Connecticut speckle program. It has a magnitude difference of less than 1 mag for the wavelengths of observation used here and is also a known double-lined spectroscopic binary. While ours is the first visual orbit based on image data resolving the two stars, there is an astrometric orbit in the literature due to Ren & Fu (2010), where the orbit was determined by examining the intermediate astrometric data from *Hipparcos*. Our orbital parameters essentially confirm and slightly improve their results. The parallax in the *Gaia* DR2 is given as $\pi = 14.4824 \pm 0.0705$ mas, which implies a mass sum of $1.83 \pm 0.14 M_{\odot}$. The system is slightly metal-poor with an

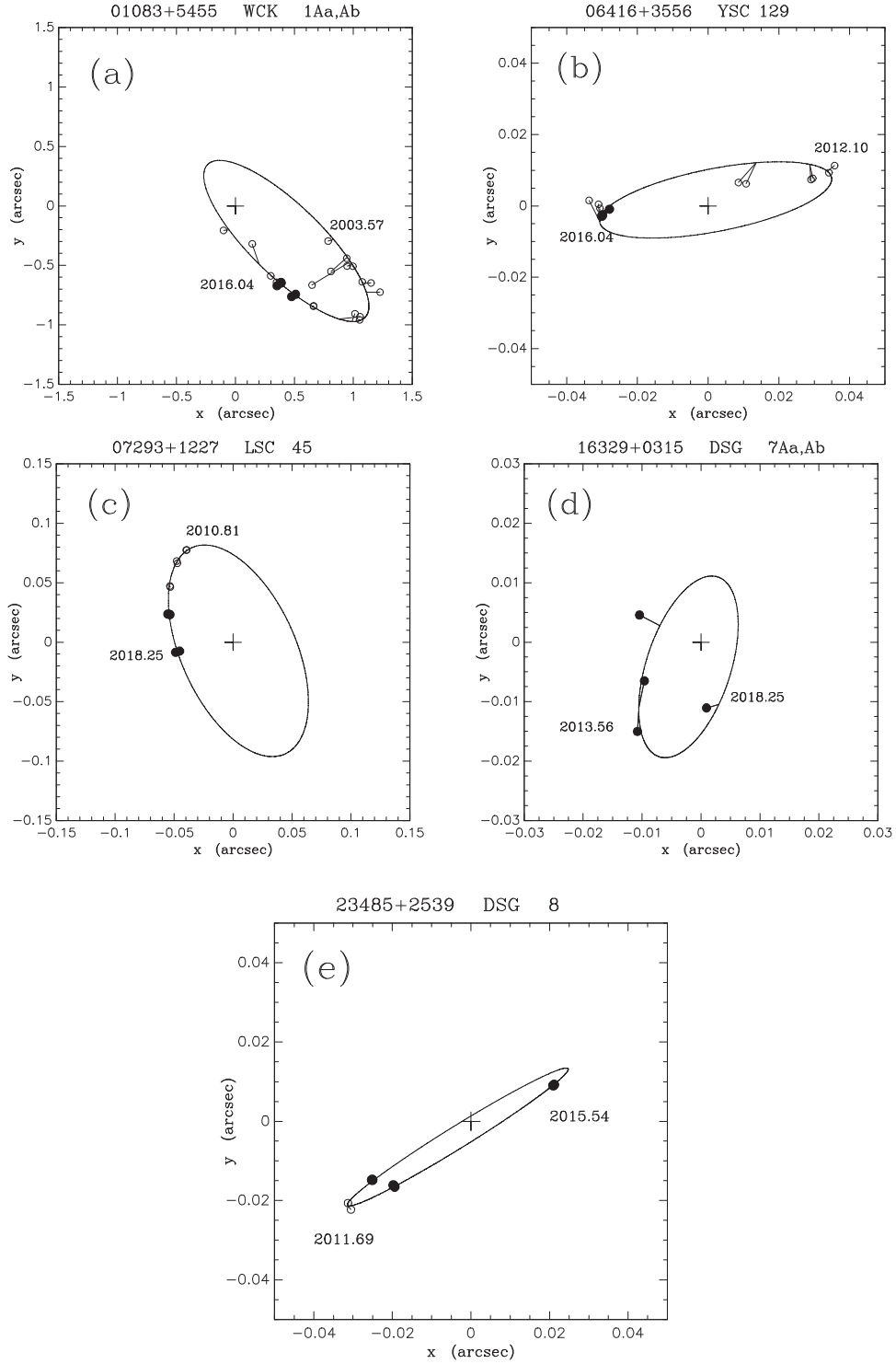


Figure 6. Visual orbits for the five systems appearing in Table 5 and described in the text. In all cases, the calculated orbit is shown as a solid line, non-Gemini observations in the literature are shown as open circles, and Gemini observations, including those presented in this paper, are shown as filled circles. A line segment is drawn from each observation to the ephemeris prediction on the orbital ellipse. (a) WCK 1Aa, Ab = HIP 5336; (b) YSC 129 = HIP 32040; (c) LSC 45 = HIP 36387; (d) DSG 7Aa, Ab = HIP 81023; and (e) DSG 8 = HIP 117415.

[Fe/H] value of -0.20 . The spectral type given in SIMBAD is F8III; based on the magnitude difference, the secondary is probably in the mid-G range. We can also derive a parallax given the spectroscopic and visual orbital elements; we obtain 13.1 ± 0.3 mas, which is almost 10% lower than the *Gaia* value. Given that there are not yet very many Gemini points on this orbit, it is possible that the semimajor axis could be biased

by the 4 m telescope data in the literature. On the other hand, the system would not have been resolved by *Gaia*, and it is possible that the acceleration of the system affects the DR2 result. Further large-aperture observations are warranted to reduce the uncertainty of the orbital parallax as we wait for future *Gaia* updates. A mass ratio of 0.952 ± 0.015 is implied

Table 6
Further Observed Properties for the Systems in Table 5

Name	HIP	π (mas)	M_V (mag)	Spectral Type	[Fe/H]	$B - V$	Δm (692 nm)
1	2	3	4	5	6	7	8
WCK 1Aa, Ab	5336	132.38 ± 0.82^a	5.78	G5V	-0.68^b	0.704 ± 0.004	5.70 ± 0.74
YSC 129	32040	14.4824 ± 0.0705	2.29	F8III	-0.20	0.509 ± 0.006	0.64 ± 0.11
LSC 45	36387	6.5387 ± 0.0614	2.09	F2	-0.52	0.438 ± 0.014	1.40 ± 0.02
DSG 7Aa, Ab	81023	24.0090 ± 0.3582	5.64	K0V	-1.39^c	0.868 ± 0.004	1.13 ± 0.16
DSG 8	117415	14.3551 ± 0.0532	2.16	F2IV-V	-0.46	0.443 ± 0.009	0.07 ± 0.02

Notes.

^a No *Gaia* DR2 parallax is available; the value shown is the revised *Hipparcos* result.

^b From Boyajian et al. (2008).

^c From Latham et al. (1992).

by the orbit; from this and the total mass, we deduce individual masses of 0.94 ± 0.07 and $0.89 \pm 0.09 M_\odot$.

4.1.3. LSC 45 = WDS 07293+1227

The orbit presented here ($P = 40.8$ yr) is the first visual orbit of this system, which does not have a spectroscopic orbit in the literature but does appear in the Geneva–Copenhagen catalog with an [Fe/H] of -0.52 and is listed as a double-lined system with a mass ratio of 0.935 ± 0.048 . The system is somewhat distant, with a parallax of 6.5387 ± 0.0614 mas provided by DR2. Thus, given our period and semimajor axis, we deduce a total mass of $1.86 \pm 0.31 M_\odot$ and individual masses of 0.96 ± 0.17 and $0.90 \pm 0.19 M_\odot$.

4.1.4. DSG 7Aa, Ab = WDS 16329+0315

We update our previous orbit that appears in Horch et al. (2015a) with a visual-spectroscopic orbit; in that work, we only had two epochs to work with that were only days apart, and thus our orbit, even when fixing the spectroscopic orbital elements to the values known from the orbit of Latham et al. (2002), was somewhat uncertain. To make matters worse, the system is of extremely small separation throughout the orbital path. Nonetheless, in Table 2, we have presented two other epochs where the system was measured, and these are consistent with the $P = 0.62$ yr orbit we previously determined. The addition of the new points allows for a better orbit and a revision of the total mass. Because this system is so challenging, with all measures below the formal diffraction limit at Gemini, we elected to average the results in the two DSSI filters from each epoch to hopefully make the orbit more robust. The system has a composite spectral type of K0V and is very metal-poor, with [Fe/H] measured as -1.4 by Latham et al. (1992). Our magnitude differences for this system should be viewed as uncertain for the reasons cited above for small-separation single-lined systems; nonetheless, this system will be discussed further Section 4.2.

4.1.5. DSG 8 = WDS 23485+2539

The only measures to date of this well-known double-lined spectroscopic binary with a period of 3.22 yr are those that we have taken at Gemini. The improved *Gaia* parallax combined with a revised orbit here lead to a much more precise total mass for the system than in our previous work; we now find $M_{\text{tot}} = 2.21 \pm 0.16 M_\odot$. A mass ratio of 1.01 ± 0.02 is implied from our orbit; thus, the individual masses are

1.10 ± 0.08 and $1.11 \pm 0.09 M_\odot$. While the spectral type in the literature is F2IV-V, the system is slightly redder than F2; we treat this system as an F5+F5.5 dwarf pair in the next section. The parallax that we can obtain from the SB+visual orbit presented is in complete agreement with the *Gaia* DR2 value: 14.3 ± 0.4 mas from our orbit versus 14.3551 ± 0.0532 mas from *Gaia*.

4.2. An Update on Metal-poor Stellar Masses

We have a significantly better understanding of the mass–luminosity relation (MLR) for main-sequence stars due to the recent work of, e.g., Torres et al. (2010) and Benedict et al. (2016), but neither of these papers includes stars that are very low in metallicity. Other studies using long-baseline optical interferometry have begun to address metallicity (e.g., Boyajian et al. 2012b, 2012a; Feiden & Chaboyer 2012), but only as low as about [Fe/H] = -0.5 . Our project at Gemini has been extending this significantly on the low-metallicity end, with the specific goal of empirically determining an MLR for metal-poor stars for the first time. As the observations in Table 2 make clear, we were able to expand the sample to the Southern Hemisphere beginning in 2016, drawing newly discovered, small-separation binary systems of interest from the active speckle program at the SOAR telescope (see, e.g., Tokovinin et al. 2018 and references therein).

In Table 6, we list some further observed properties of the five systems identified above. The columns give (1) the discoverer designation; (2) the *Hipparcos* number; (3) the *Gaia* parallax from DR2; (4) the absolute magnitude obtained from the apparent magnitude (which is not listed here) and the parallax, where no reddening correction was made because these systems are all nearby; (5) the (composite) spectral type as it appears in SIMBAD; (6) the metal abundance from Holmberg et al. (2009), unless the value is otherwise marked; (7) the $B - V$ value listed in the *Hipparcos* Catalog, and (8) the average magnitude difference at 692 nm from all available DSSI measures of the target.

Using the most recent Yale isochrones (Spada et al. 2013), we investigated the behavior of stellar mass as a function of metal abundance at fixed $B - V$ color in our previous work (Horch et al. 2015a), specifically, Figure 8 of that paper. While there is some variation depending on age and the choice of the mixing-length parameter, we found that there was little dependence on a star’s color (or, equivalently, effective temperature) over the range of interest here. We argued there that, because the curves are nearly independent of temperature,

Table 7
Mass Comparison for the Systems in Table 6

Name	HIP	Assigned Component Spectral Types and $B - V$ Colors ^a	Derived Composite $B - V$ ^a	Derived Δm at 692 nm	Derived Masses (M_{\odot}) ^a	Implied Total Mass (M_{\odot}) ^a	Total Mass from Orbit (M_{\odot})
WCK 1Aa, Ab	5336	G5V, M4.5V (0.68, 1.59)	0.68	5.62	0.92, 0.24	1.16 ± 0.07	0.906 ± 0.023
YSC 129	32040	F5IV, G5IV (0.44, 0.68)	0.49	0.43	1.4, 1.0	2.40 ± 0.14	1.83 ± 0.14
LSC 45	36387	F2V, G2V (0.35, 0.63)	0.41	1.40	1.52, 1.02	2.54 ± 0.05	1.86 ± 0.31
DSG 7Aa, Ab	81023	K1V, K6V (0.86, 1.24)	0.88	1.30	0.77, 0.64	1.41 ± 0.03	0.70 ± 0.20
DSG 8	117415	F5V, F5.5V (0.44, 0.45)	0.44	0.06	1.40, 1.37	2.77 ± 0.09	2.16 ± 0.17

Note.

^a These columns assume a solar metal abundance.

it should be true that the total mass of a binary star system will follow the same trend if both stars fall within the spectral range of the simulations.

We are now in a position to update the 2015 results with the orbits from the work here. Most of the orbits used in Horch et al. (2015a) are not in need of revision, but in Table 7, we have dynamical estimates of the total masses of the systems discussed in the previous section, which, if we combine with the previous work, gives a total of 12 systems. However, DSG 6, which was part of the sample in the 2015 paper, has been removed here for the reasons stated earlier, leaving us with 11 systems with which to refine the previous results. Besides the new orbital information for these five systems, the recent release of the *Gaia* DR2 provides much better parallaxes than we previously used in the majority of cases, and two of the orbits have been subsequently updated by other authors. These new data constrain the dynamical masses much better than was possible with the earlier results. We can therefore combine the two samples, update the parallaxes and total masses, and arrive at an improved relationship between total mass and metallicity.

The sample that we can report on now covers a range from the solar value to as low as $[\text{Fe}/\text{H}] = -1.4$. We are studying systems that are as metal-poor as $[\text{Fe}/\text{H}] = -2.01$, but some of these do not have orbital information of sufficient quality to include in this analysis. Given the measured properties of each of our binaries, the stellar models allow us to estimate the total mass of the solar-abundance binary star of the same color. We can compute the ratio of the dynamical masses we determine to the solar analog for the system and examine whether the trend is similar to what the stellar models predict. To make this mass estimate, we use the composite $B - V$ color for the system as it appears in the *Hipparcos* Catalog and the average magnitude difference measured by DSSI at 692 nm, combining all observations of the system in that filter to date at Gemini, i.e., the last two columns of Table 6. As in the previous work, we then use the solar-abundance spectral library of Pickles (1998) to combine stars of different spectral types to produce a composite $B - V$ value and Δm at 692 nm that is as close as possible to the measured values. We incorporate into these models a standard atmospheric transmission curve, the known filter transmission curve, and the dichroic transmission curve for DSSI. Table 7 repeats the identification of the targets in the first two columns; then, in the third and fourth columns, it shows the assigned component spectral types and the composite (system) $B - V$ that were obtained in this way. If the modeling is reasonably accurate, then the latter should be in good agreement with the measured $B - V$ for the system found in the literature and reported in Table 6. This is true in all cases.

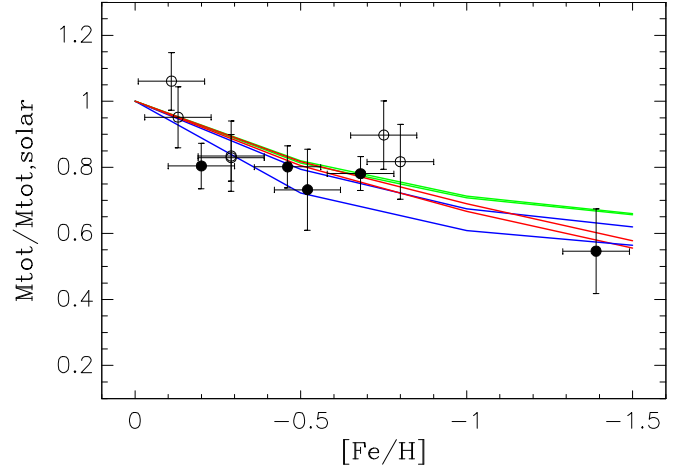


Figure 7. Observed dependence of total mass as a function of iron abundance at fixed $B - V$ color. This plot is a revision of that presented in Horch et al. (2015a), where the blue, green, and red curves represent values derived from stellar models as discussed in the text for main-sequence binaries of composite spectral type F, G, and K, respectively. There are two curves for each spectral type, for ages of 1 and 4 Gyr. The open circles represent systems that appeared in Horch et al. (2015a) with revised placement based on *Gaia* DR2 parallaxes and/or more recent orbit calculations whenever available, and the filled circles are the systems shown in Table 5 and Figure 6 (two of which also appeared in the earlier paper).

Finally, the $B - V$ value associated with the assigned spectral type of each component is converted into a mass estimate using the standard reference of Schmidt–Kaler (1982), and these appear in the sixth and seventh columns of Table 7. We have estimated the uncertainty of the total masses shown by using the scatter in the $B - V$ color. We also checked the conversion from the photometric information to mass using the information provided in the work of Boyajian et al. (2012a, 2012b) and found very good agreement with the Schmidt–Kaler reference over the spectral range of interest and assuming solar metallicity for our models. Finally, in the last column of Table 7, we show the dynamical total mass estimate using *Kepler*’s harmonic law and the data in Table 5. While it is not used in the analysis here, it is worth noting that for the systems that are double-lined spectroscopic binaries, the mass ratios m_2/m_1 implied from Table 7 are in reasonably good agreement with the values implied from the spectroscopic orbits in both cases.

In Figure 7, we plot both the theoretical and observed ratio of binary system mass to the solar-abundance value as a function of metal abundance. We have assumed an uncertainty in metallicity of the observed data of 0.1 dex (which is the uncertainty stated in Holmberg et al. 2009, the source of most

of our abundance values). The plot suggests that, within the uncertainty, the points follow the trend expected from the stellar structure calculations. In this updated plot, we have been able to shrink the vertical error bars by roughly 25%–50% in general and therefore make a more definitive statement than before concerning the good agreement between the observational data and stellar models for a wide range of metallicity, given the observational uncertainties. Furthermore, it is interesting to note that the data points usually lie closest to the model curves for the correct spectral type. While Figure 7 falls short of a true metal-poor MLR, it does allow us to include systems where no mass ratio information is available or when it is of low quality (as it is for most of the single-lined spectroscopic binaries in the sample). Thus, the value of the plot is as a tool to investigate the behavior of mass as a function of metallicity with the highest-precision information that we have at present, namely the total mass of each system. When we have determined individual masses of high precision for more of our sample and over a greater range of metallicity, we hope to construct an empirical metal-poor MLR that would give a relevant comparison to theoretical stellar models.

4.3. Triple Stars

Of the 12 new components listed in Table 2, seven were stars observed in the metal-poor program, two were part of the triple-star program, and three were serendipitous discoveries where the primary star was originally used as a point-source calibration object. In both cases for the triple-star program, the architecture of the system is Aa, Ab-B. For the metal-poor program, of the seven discoveries, two have single-lined orbits in the literature (HIP 4754 and HIP 80925), one has a double-lined orbit (HIP 81170), and four have mass ratios listed in the Geneva–Copenhagen spectroscopic catalog (HIP 19915, HIP 56851, HIP 57421, and HIP 80925), indicating that a double-lined orbit would be possible. We can infer from this that four of the seven systems are in fact triple stars, because in three cases, the separations we measure are too large to correspond to the spectroscopic component, and in the fourth, HIP 72492, we explicitly see that the system is triple in Figure 2. HIP 72492 is the sole example in this set of discoveries that is of architecture A-Ba, Bb. The seven systems span a very large range in metallicity; HIP 57421 has an $[\text{Fe}/\text{H}]$ of $+0.15$, and HIP 19915 has an $[\text{Fe}/\text{H}]$ of -2.01 , as shown in the Geneva–Copenhagen catalog.

Considering all of the triple stars in Table 2, the observations of hierarchical multiple systems presented here provide rich material for the study of their orbital architecture. Triple systems where both the outer and inner orbits are known and their relative orientation can be determined are still relatively rare. The calculation of such orbits is outside the scope of this paper, but to illustrate the power of DSSI at Gemini, we provide in Figure 8 the inner orbit of the 5 yr subsystem in WDS 16057–0617 (HIP 78849). We comment below on some remarkable hierarchies, in addition to the comments on new resolutions provided in Section 3.1.

1. WDS 11221–2447 (HIP 55505) is the young pre-main-sequence quadruple TWA 4. The double-lined subsystem Ba, Bb is resolved here. It was previously resolved only with the Keck interferometer.
2. WDS 11596–7813 (HIP 58484) is the young triple system in the ϵ Cha association composed of three B9V

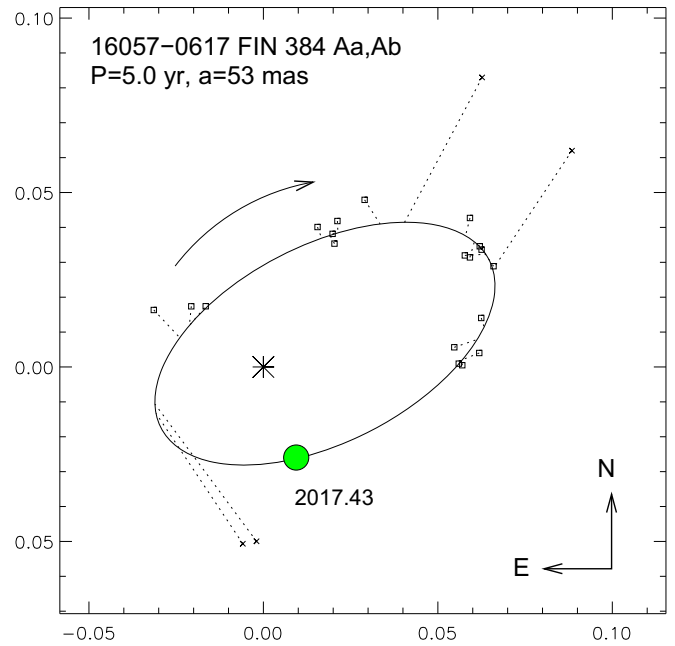


Figure 8. Inner orbit of the subsystem Aa, Ab in the triple star HIP 78849 (BU 914 AB and FIN 384 Aa, Ab). The DSSI measure is marked by the green circle on the previously unobserved part of the orbit. Four deviant measures (crosses) come from micrometer observations and speckle interferometry, illustrating the difficulty of this object. The outer orbit with a period of 311 yr is also known, and it is not coplanar with the inner orbit.

stars. Its eccentric inner orbit will soon be determined (see Figure 5 in Briceño & Tokovinin 2017).

3. WDS 14598–2201 (HIP 73385) has an astrometric subsystem in which the component with a period of 3.56 yr is not resolved here. Its previous resolutions at SOAR (TOK 47 Aa, Ab) might be spurious. This is a metal-poor triple system.
4. WDS 16120–1928 (HIP 79374) is the young hierarchical system ν Sco with seven components in the Upper Scorpius association. The resolved tight pair CHR 146 Aa, Ab has an estimated period of less than 10 yr but no orbit, so far, owing to the lack of speckle coverage.
5. WDS 16253–4909 (HIP 80448) is a young hierarchical quadruple system. We resolved the subsystem CVN 27 Ba, Bb, for which a 20 yr orbit has been computed (Tokovinin 2018). Our measurement is in excellent agreement with this orbit.
6. WDS 17157–0949 (HIP 84430) is an interesting triple system where both the inner and outer orbits are known, with periods of 5.1 and 150 yr, respectively. The orbits are not coplanar. The dynamical parallax deduced from the orbits, about 7 mas, disagrees with both *Hipparcos* (5.7 mas) and *Gaia* (2.7 mas).
7. WDS 18112–1951 (HIP 89114) has the inner subsystem TOK 57 Aa, Ab (also known from lunar occultations) with a short (~ 10 yr) period but still undefined orbit, to which our measurement contributes.
8. WDS 18126–7430 (HIP 89234) is a triple system with comparable separations (potentially interacting) and a known 324 yr outer orbit. The measurement made here allows us to compute the preliminary inner orbit of TOK 58 Aa, Ab with a period of 39 yr and high eccentricity. More data are needed to confirm this orbit and make a full dynamical study of this system.

9. WDS 19453–6823 (HIP 97196) is similar to the previous object, having comparable separations of the inner and outer subsystems. The outer orbit is not known (estimated period 40 yr), while these observations allow us to compute the preliminary inner orbit of TOK 425 Ba, Bb with a period of 4 yr.

5. Conclusions

We have presented 248 measures of close binary and trinary stars where the data were taken at the Gemini North and South telescopes over the last 3 yr using speckle imaging. The astrometric and photometric precision of this sample appears similar to that of previous papers, namely ~ 1.3 mas in separation and $\sim 0.6^\circ$ in position angle when measures in both instrument channels are averaged and ~ 0.1 mag in magnitude difference in general. However, these numbers increase somewhat when the separation is below the diffraction limit and/or the magnitude difference is above 4. The overall accuracy of our measures is affected by the uncertainty in the scale and orientation values; we find that the pixel scales used here are uncertain at approximately the 0.4% level, and that the position angle offsets are uncertain to 0.4° . To judge the overall uncertainty of any given measure, these numbers should be added in quadrature with the internal precision numbers. However, no systematic offsets in position angle or separation were noted in studying systems where independent positional information was available. Twelve previously unknown companions were discovered.









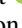

Given these measures, we computed visual orbital elements for five systems, one of which had no previous visual orbit (although it was known to be a spectroscopic binary) and the other four of which were calculated as visual-spectroscopic orbits. Using these orbits, our previous work, and recent parallax results from *Gaia*, we found it possible to refine our understanding of the effect of metallicity on the total mass of a binary and concluded that the trend in lower mass for a given spectral type for metal-poor systems predicted by stellar models remains borne out in these observations. Future observations of this kind could allow us to construct an empirical low-metallicity MLR and also to understand the role of metallicity in stellar multiplicity statistics.

Including the discovered components, we resolved 19 systems into triples, and a number of other objects we report on here are subsystems of known triples or multiples. These results have allowed us to continue the work of characterizing these systems as a part of a broader census of triples that could tell us more about star formation mechanisms in the future.

We gratefully acknowledge support from the National Science Foundation, grants AST 15-17824 and AST 16-16698, in the completion of this work. We also thank the excellent staff at both Gemini telescopes for their help and support during our observing runs. We are mindful of the fact that Maunakea is a sacred site for native Hawaiians and are grateful for the opportunity to be present there. E.H. thanks W. van Altena and P. Demarque for their continued interest in and support of this work. We thank the anonymous referee for providing a number of comments and corrections that improved the paper. These observations were taken as a part of NOAO programs 2015B-0081, 2016A-0225, and 2017A-0205. We made use of the Washington Double Star Catalog, maintained

at the U.S. Naval Observatory; the SIMBAD database, operated at CDS, Strasbourg, France; and the Ninth Catalog of Spectroscopic Orbits of Binary Stars, maintained by D. Pourbaix. We also made use of data from the European Space Agency (ESA) mission *Gaia* (<https://www.cosmos.esa.int/gaia>), processed by the *Gaia* Data Processing and Analysis Consortium (DPAC; <https://www.cosmos.esa.int/web/gaia/dpac/consortium>). Funding for the DPAC has been provided by national institutions, in particular the institutions participating in the *Gaia* Multilateral Agreement.

ORCID iDs

Elliott P. Horch  <https://orcid.org/0000-0003-2159-1463>
 Andrei Tokovinin  <https://orcid.org/0000-0002-2084-0782>
 Dana I. Casetti-Dinescu  <https://orcid.org/0000-0001-9737-4954>
 Mark E. Everett  <https://orcid.org/0000-0002-0885-7215>
 Gerard T. van Belle  <https://orcid.org/0000-0002-8552-158X>
 Steve B. Howell  <https://orcid.org/0000-0002-2532-2853>
 Lea A. Hirsch  <https://orcid.org/0000-0001-8058-7443>
 Nicholas J. Scott  <https://orcid.org/0000-0003-1038-9702>
 Rachel A. Matson  <https://orcid.org/0000-0001-7233-7508>
 Stephen R. Kane  <https://orcid.org/0000-0002-7084-0529>

References

- Benedict, G. F., Henry, T. J., Franz, O. G., et al. 2016, *AJ*, **152**, 141
 Bopp, B. W., Evans, D. S., Laing, J. D., & Deeming, T. J. 1970, *MNRAS*, **147**, 355
 Boyajian, T. S., McAlister, H. A., Baines, E. K., et al. 2008, *ApJ*, **683**, 424
 Boyajian, T. S., McAlister, H. A., van Belle, G., et al. 2012a, *ApJ*, **757**, 112
 Boyajian, T. S., von Braun, K., van Belle, G., et al. 2012b, *ApJ*, **746**, 101
 Briceño, C., & Tokovinin, A. 2017, *AJ*, **154**, 195
 DeRosa, R. J., Patience, J., Vigan, A., et al. 2012, *MNRAS*, **422**, 2765
 Docobo, J. A., & Andrade, M. 2013, *MNRAS*, **428**, 321
 Docobo, J. A., & Ling, J. F. 2009, *AJ*, **138**, 1159
 Drummond, J. D., Christou, J. C., & Fugate, R. Q. 1995, *ApJ*, **450**, 380
 ESA 1997, The Hipparcos and Tycho Catalogues (Noordwijk: ESA), *ESA SP 1200*
 Feiden, G. A., & Chaboyer, B. 2012, *ApJ*, **757**, 42
 Gaia Collaboration 2018, *A&A*, **616**, A1
 Griffin, R. F. 2013, *Obs*, **133**, 269
 Hartkopf, W. I., Mason, B. D., & Worley, C. E. 2001a, *AJ*, **122**, 3472
 Hartkopf, W. I., McAlister, H. A., & Mason, B. D. 2001b, *AJ*, **122**, 3480
 Holmberg, J., Nordström, B., & Andersen, J. 2009, *A&A*, **501**, 941
 Horch, E. P., Casetti-Dinescu, D. I., Camarata, M. A., et al. 2017, *AJ*, **153**, 212
 Horch, E. P., Franz, O. G., & van Altena, W. F. 2006, *AJ*, **132**, 2478
 Horch, E. P., Howell, S. B., Everett, M. E., & Ciardi, D. R. 2012, *AJ*, **144**, 165
 Horch, E. P., Howell, S. B., Everett, M. E., & Ciardi, D. R. 2014, *ApJ*, **795**, 60
 Horch, E. P., Meyer, R. D., & van Altena, W. F. 2004, *AJ*, **127**, 1727
 Horch, E. P., van Altena, W. F., Demarque, P., et al. 2015a, *AJ*, **149**, 5
 Horch, E. P., van Belle, G. T., Davidson, J. W., Jr., et al. 2015b, *AJ*, **150**, 151
 Horch, E. P., Veillette, D. R., Baena-Gallé, R., et al. 2009, *AJ*, **137**, 5057
 Latham, D. W., Mazeh, T., Stefanik, R. P., et al. 1992, *AJ*, **104**, 774
 Latham, D. W., Stefanik, R. P., Torres, G., et al. 2002, *AJ*, **124**, 1144
 Lohmann, A. W., Weigelt, G., & Wirmitzer, B. 1983, *ApOpt*, **22**, 4028
 MacKnight, M., & Horch, E. P. 2004, *BAAS*, **36**, 788
 Mason, B. D., Wycoff, G. L., Hartkopf, W. I., et al. 2001, *AJ*, **122**, 3466
 Matson, R. A., Howell, S. B., Horch, E. P., & Everett, M. E. 2018, *AJ*, **156**, 31
 Méndez, R. A., Claveria, R. M., Orchard, M. E., & Silva, J. F. 2017, *AJ*, **154**, 187
 Meng, J., Aitken, G. J. M., Hege, K., & Morgan, J. S. 1990, *JOSAA*, **7**, 1243
 Moe, M., Kratter, K. M., & Badenes, C. 2018, *ApJ*, submitted (arXiv:1808.02116)
 Muterspaugh, M. W., Hartkopf, W. I., Lane, B. F., et al. 2010, *AJ*, **140**, 1623
 Muterspaugh, M. W., Lane, B. F., Fekel, F. C., et al. 2008, *AJ*, **135**, 766
 Muterspaugh, M. W., Mijngaarden, M. J. P., Henrichs, H. F., et al. 2015, *AJ*, **150**, 140
 Pickles, A. J. 1998, *PASP*, **110**, 749

- Pourbaix, D., Tokovinin, A. A., Batten, A. H., et al. 2004, [A&A](#), **424**, 727
- Ren, S., & Fu, Y. 2010, [AJ](#), **139**, 1975
- Schmidt-Kaler, T. 1982, in *Stars and Star Clusters*, ed. K. Schaefers & H.-H. Voigt (Berlin: Springer), 1
- Scott, N. J., Howell, S. B., & Horch, E. P. 2016, [Proc. SPIE](#), **9907**, 99072R
- Spada, F., Demarque, P., Kim, Y.-C., & Sills, A. 2013, [ApJ](#), **776**, 87
- Tokovinin, A. 2012, [AJ](#), **144**, 56
- Tokovinin, A. 2016, ORBIT: IDL Software for Visual, Spectroscopic, and Combined Orbits, Zenodo, doi:[10.2581/zenodo.6119](#)
- Tokovinin, A. 2017, [AJ](#), **154**, 110
- Tokovinin, A. 2018, [AJ](#), **156**, 194
- Tokovinin, A., & Horch, E. P. 2016, [AJ](#), **152**, 116
- Tokovinin, A., & Latham, D. W. 2017, [ApJ](#), **838**, 54
- Tokovinin, A., Mason, B. D., & Hartkopf, W. I. 2010, [AJ](#), **139**, 743
- Tokovinin, A., Mason, B. D., Hartkopf, W. I., et al. 2015, [AJ](#), **150**, 50
- Tokovinin, A., Mason, B. D., Hartkopf, W. I., et al. 2018, [AJ](#), **155**, 235
- Tokovinin, A., Pribulla, T., & Fischer, D. 2015, [AJ](#), **149**, 8
- Torres, G., Andersen, J., & Giménez, A. 2010, [A&ARv](#), **18**, 67
- van Leeuwen, F. 2007, [A&A](#), **474**, 653